Research Square

Preprints are preliminary reports that have not undergone peer review.
They should not be considered conclusive, used to inform clinical practice,
or referenced by the media as validated information.

Multi-Excitation Front-Face Fluorescence Spectroscopy with Explainable LSTM for Detection of Lymphatic Tissue Adulteration in Ground Beef

Asima Saleem
asmagill1994@gmail.com

Yangzhou University

Muhammad Awais
Yangzhou University

Faizan ul Haq
Yangzhou University

Shuo Wang
Yangzhou University

Sheng-qi Rao
Yangzhou University

Ramdhane Koroui
Université d'Artois

Research Article

Keywords: excitation-emission matrix, explainable artificial intelligence, SHAP, lymphatic tissue, meat adulteration, external validation, LSTM

Posted Date: October 19th, 2026

DOI: https://doi.org/10.21203/rs.3.rs-11142103/v1

License: This work is licensed under a Creative Commons Attribution 4.0 International License.
Read Full License

Additional Declarations: No competing interests reported.

Abstract

Minced beef adulterated with lymphatic tissue presents food-safety, authenticity and economic concerns, optical detection is complicated by variation in fat content, lipid oxidation and muscle type that alter fluorescence independently of adulteration. We therefore combined multi-excitation front-face fluorescence with explainable long short-term memory (LSTM) network to improve specificity. A total of 824 minced beef samples from five commercial slaughterhouses, three breeds, two slaughter-age groups and three muscle cuts, were prepared; 11 spectral outliers were excluded, leaving 813 samples for analysis. Excitation-emission measurements at 280, 322, 340 and 380 nm sampled fluorescence associated with tryptophan, vitamin A, NADH, flavins, collagen cross-links and oxidation. Standard normal variate preprocessing and competitive adaptive reweighted sampling reduced the input variables from 188 to 86 channels, modelled using a shared weight four input LSTM. On the internal test set, model achieved R^2P = 0.997, RMSEP = 1.60% w/w and RPD = 19.5. External validation demonstrated performance on two previously unseen slaughterhouses (R^2P = 0.988–0.993, RMSEP = 2.60–3.35% w/w, RPD = 9.3–12.0). Interference study (n = 104) incorporating adipose tissue, saline, oxidation and muscle-cut variation, predicted lymphatic content remained below 0.5% w/w and met prespecified equivalence margin of ± 1.0% w/w. SHAP analysis identified increased NADH and reduced tryptophan associated fluorescence as influential predictors. Multi-batch detection limit was 1.8% w/w, whereas reliable quantification began at 6.0% w/w. These results support the use of multi-excitation fluorescence-LSTM analysis for screening lymphatic-tissue adulteration at concentrations relevant to the regulatory thresholds, while reliable quantification near 2% w/w and transferability across instruments remain to established

1. Introduction

Meat product authenticity reinforces food-safety regulation, consumer protection and the economic integrity of the global meat supply chain (Oleinikova *et al*., 2025; Deng *et al*., 2024; Aslam *et al*., 2023). Research has concentrated on inter-species substitution beef adulterated with pork, poultry or horsemeat, whereas the fraudulent incorporation of lymphatic tissue into ground beef remains comparatively under-investigated (Wang *et al*., 2024; Grispoldi *et al*., 2020). Lymph nodes are classified as offal rather than skeletal muscle and are excluded from most regulatory definitions of edible meat (Jadeja *et al*., 2022), and are recognised reservoirs for zoonotic pathogens including Salmonella spp. and Escherichia coli O157:H7 (Grispoldi *et al*., 2020; Vohra *et al*., 2018). Profiling of nodes recovered at a commercial abattoir has confirmed that they carry substantial and diverse bacterial loads even where Salmonella and Shiga-toxin-producing E. coli are not detected (Zhang *et al*., 2024). Detection today relies mainly on visual post-mortem inspection, which cannot identify lymphatic material once it has been incorporated into finely comminuted products (Yu *et al*., 2025; He *et al*., 2021). Where a positive identification is required, DNA and protein-based laboratory methods supply the necessary specificity (Duft *et al*., 2025; Pu *et al*., 2023; Yang *et al*., 2022), but they are destructive, depend on wet-chemical preparation and skilled operators, and are impractical as a high-throughput screen.

Spectroscopic techniques offer rapid, non-destructive, reagent free alternatives for meat quality and authenticity assessment (Li *et al*., 2020; Hassoun *et al*., 2019; Karoui & Blecker, 2011). Front-face fluorescence spectroscopy (FFFS) is well suited to turbid, opaque matrices such as minced meat because its illumination geometry avoids the inner-filter effects and reabsorption artifacts that affect conventional right-angle measurements on solid samples (Boubellouta & Dufour, 2012; Dufour *et al*., 2003). FFFS has been used to monitor muscle food freshness (Hassoun, 2021), detect inter-species adulteration (Saleem *et al*., 2022, 2024), authenticate camel milk (Boukria *et al*., 2023), discriminate muscle types (Aït-Kaddour *et al*., 2018) and monitor lipid oxidation (Hassoun, 2021; Gatellier *et al*., 2007). Most published work, uses a single excitation wavelength (≈ 280 nm, targeting aromatic amino acids), which cannot distinguish lymphatic dilution from increased intramuscular fat, lipid oxidation or muscle variability, all legitimate sources of biological noise (Fengou *et al*., 2021). Expanding the excitation range to probe multiple fluorophores, such as collagen cross-links, vitamin A, NADH coenzymes and lipid-oxidation products has been shown to improve discriminatory power (Monago-Maraña *et al*., 2021; Aït-Kaddour *et al*., 2018).

Chemometric modelling of fluorescence EEMs increasingly draws on deep-learning architectures capable of capturing non-linear spectral compositional relationships (Yuan *et al*., 2025; Zhao *et al*., 2024). Long short-term memory (LSTM) networks have outperformed PLSR and support vector machines in spectroscopic applications where adjacent wavelength channels carry correlated information (Kang *et al*., 2024; Peng *et al*., 2024) pairing them with explainable artificial intelligence keeps predictions biochemically interpretable (Dong *et al*., 2025); the SHapley Additive exPlanations (SHAP) framework, quantifies per-feature contributions on a game theoretic basis. Liu *et al*. (2025) recently combined hyperspectral imaging (HSI; 900–1700 nm) with LSTM and SHAP to map lymphatic tissue in beef, and Jiang *et al*. (2021) used near-infrared HSI to detect offal adulteration in ground pork. HSI systems substantially more expensive than fluorescence spectrometers, near-infrared range probes mainly scattering and bulk compositional absorption rather than the molecularly specific endogenous fluorophores accessible via FFFS.

The closest precedent used HSI (900–1700 nm) with LSTM and SHAP for spatial quantification. The approaches are complementary: HSI reads NIR overtones reflecting bulk composition (water, protein, fat), whereas this work exploits intrinsic fluorescence from discrete, assay verifiable biomolecules. A single-point FFFS measurement offers a potentially lower-cost configuration than a full NIR-HSI system (Dong *et al*., 2025; Wang *et al*., 2025; Yu *et al*., 2025), but returns one bulk estimate and cannot localize a small inclusion, confining it to homogeneous comminuted product, exactly the intended application. HSI retains a genuine advantage in spatial mapping. This study adds quantitative specificity data with formal equivalence testing, an excitation ablation attributing specificity to the sampling scheme, and biochemical checks across the full 0-100% dose range. Jiang *et al*. (2021) similarly showed HSI can identify offal adulteration in pork. The likely roles differ: FFFS as rapid low-cost screening, HSI for investigative characterization.

Five methodological gaps motivate the present study. First, single-batch sampling designs cannot capture the inter-farm, inter-breed and inter-animal variance that dominates real supply chains (Leng *et al*., 2023; Weng *et al*., 2020). Second, single-wavelength excitation limits specificity against non-lymphatic fluorescence variability (Saleem *et al*., 2022; Hassoun *et al*., 2019). Third, validation confined to cross-validation within one dataset tends to overestimate practical accuracy (Hassoun *et al*., 2024; Fengou *et al*., 2021). Fourth, SHAP-derived spectral interpretations are rarely checked against independent biochemical measurements (Dong *et al*., 2025). Fifth, fluorescence-based meat-authentication studies seldom report limits of detection and quantification on a defined multi-batch basis so claims of sensitivity cannot be compared across studies or against regulatory thresholds. This study addresses all five through (i) a multi-excitation EEM approach targeting five fluorophore classes, coupled with an interference study covering four non-lymphatic confounders and an excitation-ablation experiment that tests whether the multi-excitation sampling scheme itself confers the observed specificity; (ii) a five-farm, sample representing three commercial breeds (iii) two independent external validation sets from unseen slaughterhouses; (iv) biochemical corroboration of the SHAP-identified features on paired aliquots and across a full 0-100% dose series; and (v) IUPAC-consistent LOD and LOQ estimation with lack of fit testing and a weighted regression sensitivity analysis.

2. Materials and Methods

2.1. Experimental Design and Sample Collection

To ground the model in real world variability, we built a multi-strata cohort of 824 minced beef samples drawn from five independent commercial slaughterhouses (Farms A-E), chosen to reflect differences in husbandry, feed and breed composition. Samples covered three commercial breeds, two slaughter age groups (18–24 and 30–36 months) and three muscle cuts (Longissimus lumborum, Semimembranosus, Biceps femoris). Lymphatic tissue came from superficial cervical, popliteal and mesenteric nodes, pooled in equal proportions to mimic the mixed node contamination typical of industrial processing. Table 1 summarises the sample allocation, and Fig. 1 outlines the workflow from collection to model interpretation.

Adulteration was prepared gravimetrically at 0, 2, 5, 10, 15, 20, 30, 60 and 100% w/w. The calibration and internal validation cohort comprised 540 samples from Farms A-C (9 levels × 10 preparations × 3 cuts × 2 age groups). Two external sets, Farm D, Shandong (n = 90) and Farm E, Sichuan (n = 90), came from entirely unseen farms and were held out from training, preprocessing, feature selection and tuning. A separate interference set (n = 104) tested adipose addition, saline dilution, muscle-cut identity and accelerated oxidation (3, 7 and 10 days at 4°C) (Hassoun, 2021; Gatellier *et al*., 2007), benchmarked against one shared authentic-beef control across 13 conditions. Thirty additional samples for the biochemical dose series (Section 2.6) were prepared independently and excluded from the 824 samples. Two constraints shape interpretation: breed is nested within farm, so breed and farm effects cannot be separated and each replicate was an independent gravimetric blend from its own tissue pool (one patty scanned per blend, distinct from the three technical spectra averaged within each scan; Section 2.2),

rather than a subsample of a shared homogenate. Every sample was minced to 5 mm, formed into 30 g patties and equilibrated at 4 ± 0.5°C for 30 min before scanning (Hassoun *et al*., 2019). The distribution of preparations across the design cells is given in Table S13.

Table 1
Allocation of the 824 samples prepared for this study.

Sample set	Source	Composition	n prepared	n analyzed
Calibration + internal validation	Farms A-C	9 levels × 10 preparations × 3 cuts × 2 ages	540	529
- calibration subset	Farms A-C	Kennard-Stone, 70%	-	370
- internal test subset	Farms A-C	Kennard-Stone, 30%	-	159
External Set A	Farm D (Shandong)	9 levels × 5 preparations × 2 ages	90	90
External Set B	Farm E (Sichuan)	9 levels × 5 preparations × 2 ages	90	90
Interference set	Farms A-C	adipose 3 × 8; saline 3 × 8; cuts 3 × 8; oxidation 3 × 8; shared control 1 × 8	104	104
Total	Farms A-E	-	824	813

Eleven samples (2.0% of the 540–sample calibration cohort) were removed as spectral outliers before partitioning (Section 2.3); no outliers were removed from the external or interference sets. “Preparations” are independent gravimetric blends from independently sourced tissue pools. The 30 samples used for the biochemical dose series (Section 2.6) were prepared separately and are not included in this total.

2.2. Front-Face Fluorescence Spectroscopy and Data Acquisition

Fluorescence was measured on a FluoroMax-4 spectrofluorometer (Horiba Scientific, Kyoto, Japan) with a front-face fibre-optic probe held at 56° to the sample-surface normal, an angle chosen to suppress specular reflectance and inner-filter effects (Dufour *et al*., 2003) Supplementary Figure S2. Exploratory excitation-emission matrices were scanned from 250 to 400 nm in 5 nm steps with emission recorded at 300–800 nm (1 nm resolution); the four diagnostic excitation wavelengths used for modelling (280, 322, 340 and 380 nm) were then set directly. Photomultiplier-tube (PMT) voltage was tuned per sample to exceed 1000:1 signal-to-noise without saturation, per-sample adjustment the subsequent SNV normalization renders immaterial. All spectra used 0.1s integration, three accumulations and 5 nm excitation/emission slits, held constant throughout. Ultrapure-water blanks collected each session were

subtracted to remove Raman and Rayleigh scattering, including the water-Raman band near 310 nm that would otherwise intrude on the 280 nm emission window. Three replicates were averaged per sample.

Four excitation slices were chosen a priori on biochemical grounds (Aït-Kaddour *et al*., 2018; Karoui & Blecker, 2011): 280 nm for tryptophan, tyrosine and phenylalanine; 322 nm for retinol and its esters with FRET cross-peaks (Hassoun *et al*., 2019); 340 nm for NADH and flavin coenzymes (Gatellier *et al*., 2007); and 380 nm for collagen cross-links (pyridinoline, advanced glycation end-products) alongside lipid-oxidation Schiff bases (Monago-Maraña *et al*., 2021; Eyre *et al*., 2010). Truncating each slice to its informative emission window at 1 nm resolution (Em 305–351, 336–382, 440–486, 410–441 and 514–528 nm) Table S1 gave 47 channels per slice and 188 candidate variables in total.

2.3. Spectral Preprocessing and Dataset Partitioning

Four preprocessing routes were benchmarked with preliminary PLSR models: Savitzky-Golay smoothing (second-order polynomial, 11-point window), SNV, MSC and polynomial baseline correction (Rinnan *et al*., 2009). All parameters (SNV scaling factors, MSC reference spectra) were estimated on calibration s*et al*one and applied unchanged elsewhere, closing off a common leakage route. Outliers were flagged by Monte Carlo cross-validation (Kvalheim *et al*., 2019) Table S7: across 1000 iterations calibration cohort was split 80/20, and each sample accumulated mean squared prediction residual and leverage over the iterations in which it fell in the validation subset. Samples exceeding the 97.5th residual percentile and twice the mean leverage were dropped, so that 11 of 540 (2.0%) were removed and 529 retained. These were split 70/30 into calibration (n = 370) internal test (n = 159) sets by Kennard-Stone, uniform coverage of the spectral space (Han *et al*., 2021) Table S8. Preprocessing and variable selection were ranked by 10-fold RMSECV within the calibration set, never by internal-test performance; the ranking proved identical under both criteria, so the choice was not an artifact of one partition (Tables S2 and S3).

2.4. Feature Selection and Chemometric Modelling

Competitive adaptive reweighted sampling (50 Monte Carlo runs, 10-fold CV) trimmed the 188 channels to 86, outperforming UVE, VCPA and bootstrap resampling on the same SNV data (Han *et al*., 2021; Lee & Lee, 2021; Rinnan *et al*., 2009) Table S3. Four regressors of increasing complexity were compared: PLSR as a linear baseline, LSSVM with an RBF kernel (Zhang & Yang, 2025; Üstün *et al*., 2007), a 1D-CNN (two blocks, 32 and 64 filters, kernel 5, global average pooling) (Zhao *et al*., 2024; Li *et al*., 2023), and a four-input LSTM. In the LSTM each excitation slice enters as a sequence ordered along its own emission axis, fed to a shared two-layer encoder (128 units, dropout 0.30; then 64 units) whose weights are tied across slices; the four 64-unit hidden states are concatenated and passed to a dense output layer (Kang *et al*., 2024; Peng *et al*., 2024) Supplementary Figure S1. Presenting slices as separate sequences preserves the physical ordering of emission channels without the artificial step-jumps that concatenation would create. Shared weights cut trainable parameters by roughly three-quarters, which matters at n = 370; they enforce one spectral-to-latent mapping so hidden states comparable; and they let the model pool evidence across fluorophore-sharing wavelengths, the mechanism ablation in Section 3.5 tests.

2.5. Model Training, Hyperparameter Selection and Evaluation Protocol

Networks were trained with the Adam optimizer (learning rate = 0.001), batch size 32, up to 300 epochs, with early stopping (patience 20 epochs, minimum delta 0.0001) on a 74-sample validation subset drawn from the calibration set by stratified random sampling across the nine gravimetric levels and fixed across seeds. Hyperparameters (units {64, 128}, dropout {0.20, 0.30, 0.40}, learning rate {5×10^{-4}, 1×10^{-3}}) were ranked by RMSECV (Table S10). Training was repeated over five random seeds; reported metrics are seed-averaged, with a seed-to-seed RMSEP SD of 0.07% w/w. The internal test and both external sets were touched once, for final evaluation, and informed no decision at any stage.

2.6. Explainable AI: SHAP Analysis and Biochemical Validation

Interpretability used SHAP with the Deep Explainer module against a 100-spectrum k-means background; mean absolute SHAP values ranked global feature importance (Dong *et al*., 2025). We treat these attributions as correlational: hypotheses about which fluorophores drive predictions, tested against independent chemistry rather than asserted as causal. Four assays did that testing on parallel aliquots of the scanned samples, so each biochemical value pairs with the mean SHAP contribution of its fluorophore window: hydroxyproline as a collagen surrogate, free tryptophan by RP-HPLC, NADH fluorescence (Ex 340/Em 460 nm) and TBARS as nmol MDA/g (Gatellier *et al*., 2007). Endpoint comparison used 40 paired observations (20 at 0%, 20 at 100%), correlated at $\alpha = 0.01$. HPLC was verified in house: linear over 0.5–50 µg/mL ($r^2 > 0.999$), recovery 96–103%, and intra- and inter-day RSD below 3% and 5%; hydroxyproline (94–104%) and TBARS (97–105%) were checked in the same way (Table S5). Because agreement at the extremes cannot show continuous tracking, an independent dose series at 0, 25, 50, 75 and 100% w/w (n = 6 per level, 30 samples) was prepared separately from the 824-sample study; 12 samples are shared endpoint batches, with 18 newly prepared at intermediate levels, and a sensitivity analysis on those 18 alone confirmed the correlations do not rest on the shared endpoints (Table S6).

2.7. Analytical Sensitivity: Limit of Detection and Limit of Quantification

LOD and LOQ followed the IUPAC calibration curve method ($LOD = 3s_0/b$; $LOQ = 10s_0/b$) on a low-level calibration built from 0, 2 and 5% (w/w) samples of all five commercial slaughterhouses (n = 45). Regressing predicted on reference values gave $b = 0.967$ and $s_o = 0.58\%$ w/w (Table S9). Residual variance typically grows with concentration, estimates were re-derived by weighted least squares (weights proportional to $1/x^2$), and three-level design allowed an explicit lack-of-fit test.

2.8. Model Performance Metrics and Statistical Analysis

Performance reported as R^2P, RMSEP and the residual prediction deviation RPD = SD/RMSEP, where SD is the standard deviation of the reference values of the set in question. All three validation sets span the same nine levels in equal or near-equal numbers, giving an identical reference SD of 31.2% w/w and making R^2P, RMSEP and RPD mutually checkable ($R^2P = 1 - (RMSEP/SD)^2$). RPD thresholds followed convention: 2.0-2.5 (screening), 3.0-4.9 (quality control), ≥ 5.0 (excellent) (Rinnan *et al*., 2009). Specificity was assessed with two complementary statistics: one-way ANOVA with Tukey's HSD comparing predicted lymphatic content across interference conditions against the 0% control (R^2 is undefined here, since every interference sample has a true lymphatic content of 0%), and equivalence testing against a pre-specified margin of Δ = ±1.0% w/w; the largest TOST p was 0.021, with all 90% CIs inside ± 0.53% w/w. Group differences in the biochemical assays were tested by Student's t-test with Bonferroni correction. Analyses performed in R v4.3.2 and Python v3.11 (scikit-learn, TensorFlow 2.14, SHAP 0.44).

3. Results

3.1. Spectral Characterization: Multi-Fluorophore EEM Profiles

Analysis of the full EEMs revealed biochemically distinct spectral profiles for pure beef, adulterated mixtures and pure lymphatic tissue (Fig. 2). Pure lymphatic tissue did not show a simple proportional attenuation of the beef EEM, a finding that separates lymphatic detection from generic dilution effects. Lymphatic tissue showed substantially lower fluorescence in the tryptophan region (Ex 280/Em 340 nm; lower myofibrillar protein content) and the collagen cross-link region (Ex 380/Em 420–440 nm; consistent with reduced collagen relative to muscle), but markedly higher fluorescence in the NADH region (Ex 340/Em 460 nm; consistent with higher metabolic activity and mitochondrial density in lymphoid cells) and the lipid-oxidation-product region (Ex 380/Em 520 nm) (Monago-Maraña *et al*., 2021; Eyre *et al*., 2010; Gatellier *et al*., 2007). These bidirectional changes reductions in some fluorophore bands alongside increases in others give a multi-feature biochemical fingerprint that a simple fat or water dilution could not reproduce (Hassoun *et al*., 2019; Boubellouta & Dufour, 2012). Progressive adulteration from 0 to 100% produced systematic, monotonic changes across all four spectral regions. This monotonicity is quantified directly by the predicted versus reference linearity of Fig. 3 across all nine gravimetric levels, and at the biochemical level by the dose series of Supplementary Figure S3 and Table S6, rather than resting on the three EEM panels shown here, which are selected to illustrate the endpoint and intermediate spectral signatures.

3.2. Optimization of Spectral Preprocessing and Variable Selection

SNV transformation gave the best performance (RMSECV = 3.35%; R^2P = 0.987; RMSEP = 3.55%; RPD = 8.8), ahead of MSC (RPD = 7.7), baseline correction (RPD = 6.6), SG smoothing (RPD = 5.8) and raw spectra (RPD = 5.3; Table S2). SNV removes multiplicative light-scattering variation arising from

differences in surface topology and patty density, which suits turbid solid matrices (Weng *et al*., 2020; Rinnan *et al*., 2009), and was used for all subsequent analyses. CARS identified 86 informative channels from the 188 candidates (a 54% reduction in dimensionality), which fall within five biochemically coherent windows rather than filling them contiguously: tryptophan emission (Ex 280/Em 330–350 nm; 21 channels), vitamin A emission (Ex 322/Em 358–375 nm; 18), NADH emission (Ex 340/Em 452–475 nm; 24), and the two 380 nm windows for collagen cross-links (Ex 380/Em 416–440 nm) and lipid-oxidation products (Ex 380/Em 516–532 nm), which toget.0, account for 23 channels. As shown in Table S3, CARS gave the best balance of parsimony and accuracy (RMSECV = 2.90%; R^2P = 0.990; RMSEP = 3.08%; RPD = 10.1), ahead of bootstrap resampling, VCPA and UVE (Lee & Lee, 2021; Khamsopha *et al*., 2021). Selection stability was assessed by repeating the CARS procedure over its 50 Monte Carlo runs and retaining only those channels selected in at least 90% of runs; 78 of the 86 channels (91%) met this threshold, and the RMSECV obtained with the stability-filtered subset (2.93%) was within 1% of that obtained with the full subset (2.90%), indicating that the selected variables are not an artifact of individual resampling draws (Table S3).

3.3. Comparative Model Performance and Multi-Level Validation

Predictive performance across the validation tiers is summarised in Table 2. The LSTM led PLSR, LSSVM and1D-CNN throughout, consistent with its ability to capture long range dependencies between adjacent emission channels within each slice (Kang *et al*., 2024; Peng *et al*., 2024). On the internal test set it reached R^2P = 0.997, RMSEP = 1.60% w/w and RPD = 19.5. Its margin over the 1D-CNN however, was consistent in direction but small in size: ΔR^2P = 0.001 internal, 0.003 on External Set A and 0.004 on External Set B. A paired bootstrap of squared prediction errors (10,000 resamples) found the gap significant on both external sets (p = 0.018 and 0.011) but not internally (p = 0.21). The LSTM is therefore retained as the primary model, though the CNN remains a reasonable choice where simplicity matters.

The external sets are the harder test, and the model held up: R^2P = 0.993, RMSEP = 2.60% w/w, RPD = 12.0 on Farm D (Shandong), and R^2P = 0.988, RMSEP = 3.35% w/w, RPD = 9.3 on Farm E (Sichuan). Both stay in the excellent band (≥ 5.0), but at roughly half the internal RPD a drop consistent with real inter-farm biological variability rather than overfitting, a distinction a cross-validation only design could not have made (Leng *et al*., 2023; Weng *et al*., 2020). Reference versus predicted plots were near unity across all tiers (Fig. 3). Bootstrap-derived 95% CIs (Table S12) confirm the decline is genuine, not noise: internal and external intervals do not overlap. Seed to seed RMSEP variation (0.07% w/w) is an order of magnitude smaller than these intervals, so model instability contributes little beside sampling variability. The cause discussed in Section 4.2.

Table 2
Predictive performance of the four regression models across the internal test set and the two external validation sets.

Validation set	Metric	PLSR	LSSVM	1D-CNN	LSTM
Internal test set (n = 159)	R^2P	0.990	0.993	0.996	0.997
	RMSEP (%)	3.08	2.52	2.04	1.60
	RPD	10.1	12.4	15.3	19.5
External Set A (Farm D, n = 90)	R^2P	0.983	0.987	0.990	0.993
	RMSEP (%)	4.10	3.55	3.05	2.60
	RPD	7.6	8.8	10.2	12.0
External Set B (Farm E, n = 90)	R^2P	0.972	0.978	0.984	0.988
	RMSEP (%)	5.20	4.60	3.95	3.35
	RPD	6.0	6.8	7.9	9.3

PLSR, partial least squares regression; LSSVM, least–squares support vector machine; 1D–CNN, one–dimensional convolutional neural network; LSTM, long short–term memory. Reference SD = 31.2% w/w in each set, so R^2P, RMSEP and RPD are mutually consistent; the LSTM gives the lowest RMSEP in every tier. Metrics are the mean across five random seeds. The interference set is reported separately in Table S4 using comparison–of–means and equivalence statistics, because every interference sample has a true lymphatic content of 0% and R2 against a constant reference is undefined.

3.4. Specificity Testing Against Non-Lymphatic Interferents

The model proved highly selective for lymphatic tissue (Table S4; Fig. 4). Challenged with up to 30% adipose tissue which suppresses tryptophan fluorescence through dilution it predicted just 0.16–0.21% lymphatic content; saline dilution gave 0.14–0.31%, storage up to 10 days gave 0.18–0.48%, and muscle-cut variation gave 0.11–0.17%. One-way ANOVA found no difference among the thirteen conditions (n = 104; $F(12, 91) = 1.18$; $p = 0.31$), and Tukey HSD comparisons against the 0% control were non-significant throughout. Since a null result is not evidence of equivalence, the data were re-tested by TOST against a pre-specified ± 1.0% w/w margin: every condition passed (largest TOST $p = 0.021$), with all 90% CIs inside ± 0.53% w/w. The set therefore supports equivalence, not merely the absence of a detected difference. Two caveats apply. Interferents were tested one at a time, so combined effects elevated fat alongside advanced oxidation, for instance remain untested; and at n = 8 per condition the test detects differences of about 0.15% w/w, comfortably inside the ± 1.0% margin yet unable to exclude a smaller systematic bias. The shared control's suitability was confirmed by comparing its prediction (0.12 ± 0.09%) with 0%

samples from the calibration cohort and both external sets (ANOVA, p = 0.42), showing it represents authentic beef across the biological strata used.

3.5. Excitation Ablation: Is Multi-Excitation Sampling Responsible for the Specificity?

Specificity might have come from the LSTM architecture rather than the sampling scheme. To separate the two, the identical shared-weight architecture was retrained four times, each receiving just one excitation slice, then challenged with the same interference set (Table 3; Table S11).

Restricting the model to the conventional 280 nm excitation degraded accuracy markedly (R^2P = 0.919; RMSEP = 8.90% w/w; RPD = 3.5) and, more tellingly, produced grossly biased predictions: 3.9–6.8% apparent lymphatic content under adipose and saline challenge, and up to 4.1% after accelerated oxidation (all p < 0.001 versus control). The 322, 340 and 380 nm slices used alone were similarly non-specific. Only the four-excitation model was both accurate and unbiased, identifying multi-excitation sampling, not the deep-learning architecture, as the source of specificity. The single-excitation models expose a clean trade-off. The 280 nm slice was the most accurate but the most biased; 322 nm was the least accurate yet the least biased; 340 nm sat between them on both axes. No single slice delivers both. The slice carrying the strongest quantitative signal tryptophan at 280 nm is also the one most confounded by non-specific protein dilution, while the less-confounded slices carry weaker quantitative information. Combining them resolves the tension: four-excitation model keeps 280 nm's quantitative strength while borrowing specificity from 322, 340 and 380 nm, the core mechanistic case for multi-excitation sampling.

Table 3
Ablation of the excitation dimension. Identical shared-weight LSTM architecture, varying only the excitation slices supplied as input. Internal test set, n = 159.

Input excitation slice(s)	Channels after CARS	R^2P	RMSEP (%)	RPD	Predicted lymphatic content under interferents (% w/w, range)
Ex 280 nm only	21	0.919	8.90	3.5	3.9–6.8
Ex 322 nm only	18	0.842	12.40	2.5	1.1–2.4
Ex 340 nm only	24	0.905	9.60	3.3	2.2–4.1
Ex 380 nm only	23	0.880	10.80	2.9	1.8–3.6
All four excitations	86	0.997	1.60	19.5	0.11–0.48

Per–condition interferent predictions for single–excitation models are given in Table S11. All single–excitation models differed significantly from the 0% control under adipose, saline and oxidation challenge (Tukey HSD, p < 0.001); only the four–excitation model passed equivalence testing.

3.6. SHAP-Based Model Interpretability and Biochemical Corroboration

SHAP revealed a biochemically coherent picture of what the model keys on (Fig. 5). Two features dominate: the NADH band (Ex 340/Em 452–475 nm), whose positive effect means more NADH pushes the prediction up, and the tryptophan band (Ex 280/Em 330–350 nm), whose negative effect means less tryptophan does the same. Secondary contributions came from collagen cross-links (Ex 380/Em 416–440 nm, negative) and lipid oxidation products (Ex 380/Em 516–532 nm, positive), with vitamin A (Ex 322/Em 358–375 nm) play a modest part consistent with muscle carrying more retinol than lymphoid tissue (Hassoun *et al*., 2019). The profile matches lymphatic tissue as it actually is: metabolically active, protein-poor, collagen-poor and prone to lipid oxidation (Monago-Maraña *et al*., 2021; Eyre *et al*., 2010).

These attributions were then tested against chemistry rather than trusted on their own (Table S5). Relative to pure beef, 100% lymphatic tissue showed significantly lower tryptophan (0.98 ± 0.07 vs. 1.34 ± 0.09 mg/g; $p < 0.001$) and hydroxyproline (0.41 ± 0.05 vs. 0.92 ± 0.06 mg/g; $p < 0.001$), alongside higher NADH fluorescence (188 ± 14 vs. 112 ± 9 a.u.; $p < 0.001$) and TBARS (0.86 ± 0.09 vs. 0.41 ± 0.05 nmol MDA/g; $p < 0.001$) (Gatellier *et al*., 2007). Assays ran on parallel aliquots of the scanned samples, each value paired with the mean SHAP contribution of its fluorophore window across 40 observations; correlations were strong and correctly signed for all four markers ($|r| = 0.91–0.94$, $p < 0.001$). Limiting the analysis to the 18 newly prepared intermediate samples (25, 50 and 75%) gave $|r| = 0.94–0.97$ ($p < 0.001$), confirming the monotonic dose-response is not an artifact of shared endpoints.

Agreement at the two extremes does not show that the markers track adulteration continuously, so an independent dose series was assayed at 0, 25, 50, 75 and 100% (w/w) lymphatic tissue (n = 6 independent preparations per level; Table S6, Supplementary Figure S3). All four markers changed monotonically and near-linearly across the range, with correlations against gravimetric adulteration level of $|r| = 0.96–0.98$ (n = 30 per marker, $p < 0.001$; the 0% and 100% levels are the shared endpoint batches described in Section 2.6). The endpoint values of the dose series reproduced those of Table S5, and the direction of every marker matched the sign of the corresponding SHAP effect. The biochemical corroboration therefore holds across the 0-100% range, not only at its endpoints.

3.7. Analytical Sensitivity: Limit of Detection and Limit of Quantification

The IUPAC method applied to the low-level regression (0, 2 and 5% w/w; n = 45) gave b = 0.967 and S_o = 0.58% w/w, yielding LOD = 1.8% w/w and LOQ = 6.0% w/w (Table S9). These exceed the 1.17% LOD of an earlier single-batch study (Saleem *et al*., 2024), as expected once real inter-farm variance raises the noise floor. Robustness checks agreed closely: weighted fitting (weights $\propto 1/x^2$) gave 1.7% and 5.7%; including the 10% level (n = 60) gave 1.9% and 6.3%; a pure-error lack-of-fit test was non-significant ($F = 1.38$; $p = 0.26$). The conservative unweighted values are reported. Critically, the 1.8% LOD sits below the ~ 2% w/w discussed as an indicative action threshold (Wang *et al*., 2024; Fengou *et al*., 2021), but the

6.0% LOQ does not, so at 2% w/w the method detects but cannot reliably quantify. No single regulatory instrument specifies that threshold; it is used here as a literature-derived benchmark, not a compliance limit.

4. Discussion

4.1. The Mechanistic and Analytical Case for Multi-Excitation Fluorescence

Single-excitation work at 280 nm tracks total aromatic amino acid fluorescence, which falls with any dilution of muscle protein regardless of diluent (Saleem *et al*., 2022; Aït-Kaddour *et al*., 2018). The ablation shows a more flexible regressor cannot repair this: the same LSTM on the 280 nm slice alone predicted 3.9–6.8% apparent lymphatic content under 10–30% adipose or saline and up to 4.1% after oxidation, versus 0.11–0.48% for the four-excitation model on identical samples. SHAP suggests why: the model keys on a joint pattern (lower tryptophan and collagen alongside higher NADH and oxidation products) that fat or water dilution cannot reproduce (Boukria *et al*., 2023; Monago-Maraña *et al*., 2021; Eyre *et al*., 2010). The interference study tests this directly: adipose and saline challenges are deliberate fat and water dilution experiments over the same 10–30% range where a genuine signal must appear, and the model returned 0.14–0.31%, equivalent to control. Nor is this simply more channels: single excitation models trade accuracy against specificity, and only the four-excitation combination achieves both.

4.2. External Validation and Its Limits as A Criterion for Practical Applicability

The internal to external drop (RPD 19.5 → 9.3–12.0) is the familiar chemometric trap: single batch models absorb farm, breed or instrument specific variance that k-fold CV cannot expose, since training and test samples share it (Yuan *et al*., 2025; Fengou *et al*., 2021; Weng *et al*., 2020). Two geographically independent held-out farms (Shandong, Sichuan) are a stricter test, and external RPDs of 9.3–12.0 show the LSTM learned generalizable features (Pu *et al*., 2023; Khamsopha *et al*., 2021), still uncommon in food-spectroscopy work and a reasonable bar for regulatory consideration (Hassoun *et al*., 2024; Aslam *et al*., 2023; He *et al*., 2021). Three explanations can be separated. Overfitting is largely excluded: no external sample touched preprocessing, feature selection, tuning or early stopping, and the five-seed RMSEP spread was 0.07% w/w. Genuine inter-farm biology is what the design supports, since Set B (Sichuan) is systematically worse than Set A across all four model families a shared batch effect, not model instability. A reference-values effect is excluded by the gravimetric design. Two farms though are not the supply chain; breeds, feed regimes and practices beyond these five are untested and no literature baseline exists to calibrate the drop's size, since failed external validations rarely get published. The LSTM's edge over the CNN is real but small enough that the simpler model still merits consideration where inference cost matters.

4.3. Biochemical Interpretation and The Role of Lymphoid Cell Biology

The fingerprint reduced tryptophan and collagen fluorescence, elevated NADH and oxidation products that fits lymphoid biology. Lymph nodes comprise lymphocytes, dendritic cells, macrophages and a reticular stroma rather than the myosin, actin and troponin that dominate muscle (Li *et al*., 2019) explaining lower tryptophan (0.98 vs. 1.34 mg/g); organised perimysial and endomysial collagen, source of pyridinoline fluorescence, is largely absent (Monago-Maraña *et al*., 2021; Eyre *et al*., 2010), explaining lower hydroxyproline (0.41 vs. 0.92 mg/g). Elevated NADH matches mitochondrial density of immunologically active cells, and immunometabolism supports it: activated lymphocytes and macrophages reprogramme toward glycolysis with greater mitochondrial mass and NADPH turnover (Buck *et al*., 2017; Pearce & Pearce, 2013). Higher TBARS fits the lipid content of adipose-associated nodes and the pro-oxidant phagocytic environment (Wang *et al*., 2024; Gatellier *et al*., 2007).

5. Conclusion

This study developed a multi-excitation front-face fluorescence spectroscopy (FFFS) method combined with an explainable LSTM model to detect lymphatic tissue adulteration in ground beef. The method was evaluated using samples from five commercial slaughterhouses, covering three breeds, two slaughter ages, and three muscle cuts. The main strength of the approach is its use of four excitation wavelengths to capture different fluorescence-related signals, improving specificity compared with a single-excitation approach. Equivalence testing and excitation-ablation experiments further showed that the improved performance was mainly due to multi-excitation sampling rather than the model architecture alone. The method performed well on two independent external datasets from previously unseen slaughterhouses, with R^2P values of 0.988–0.993, RMSEP of 2.60–3.35% w/w, and RPD of 9.3–12.0. SHAP analysis was also supported by independent measurements of hydroxyproline, tryptophan, NADH, and TBARS across the adulteration range. The detection limit was 1.8% w/w, while the quantification limit was 6.0% w/w. Therefore, although the method can detect adulteration near the 2% level, reliable quantification at this concentration is not yet supported. The method is best considered a screening tool, with important or positive results requiring confirmation by an established analytical method.

Further validation is needed, like instrument-transfer studies, testing of processed beef products, broader multi-slaughterhouse and multi-laboratory validation, and reproducibility studies. Preliminary cost comparison also suggests that benchtop spectrofluorometers may have a lower initial cost than turnkey NIR-HSI systems, although a formal economic analysis is still needed.

Declarations

Author Contribution

*Asima Saleem: Conceptualization, Investigation, Data curation, Visualization, Writing-original draft. *Muhammad Awais: Conceptualization, Data curation, Visualization, Writing original draft, Writing review & editing. Faizan ul Haq: Visualization, Software, Writing-review & editing. Shuo Wang: Writing review & editing. Shengqi Rao: Supervision, Writing review & editing. Ramdhane Koroui: Investigation, Data curation, Writing review & editing.*Asima Saleem and Muhammad Awais contributed equally to this work.

References

1. Aït-Kaddour, A., Loudiyi, M., Ferlay, A., & Gruffat, D. (2018). Performance of fluorescence spectroscopy for beef meat authentication: Effect of excitation mode and discriminant algorithms. Meat Science, 137, 58–66. https://doi.org/10.1016/j.meatsci.2017.11.002.
2. Aslam, R., Sharma, S. R., Kaur, J., Panayampadan, A. S., & Dar, O. I. (2023). A systematic account of food adulteration and recent trends in the non-destructive analysis of food fraud detection. Journal of Food Measurement and Characterization, 17(3), 3094–3114. https://doi.org/10.1007/s11694-023-01846-3.
3. Boubellouta, T., & Dufour, É. (2012). Cheese-matrix characteristics during heating and cheese melting temperature prediction by synchronous fluorescence and mid-infrared spectroscopies. Food and Bioprocess Technology, 5(1), 273–284. https://doi.org/10.1007/s11947-010-0337-1.
4. Boukria, O., Boudalia, S., Bhat, Z. F., Hassoun, A., & Aït-Kaddour, A. (2023). Evaluation of the adulteration of camel milk by non-camel milk using multispectral image, fluorescence and infrared spectroscopy. Spectrochimica Acta Part A: Molecular and Biomolecular Spectroscopy, 300, 122932. https://doi.org/10.1016/j.saa.2023.122932.
5. Buck, M. D., Sowell, R. T., Kaech, S. M., & Pearce, E. L. (2017). Metabolic instruction of immunity. Cell, 169(4), 651–665. https://doi.org/10.1016/j.cell.2017.04.004.
6. Deng, Z., Wang, T., Zheng, Y., Zhang, W., & Yun, Y.-H. (2024). Deep learning in food authenticity: Recent advances and future trends. Trends in Food Science & Technology, 144, 104344. https://doi.org/10.1016/j.tifs.2024.104344.
7. Dong, F., Ma, Z., Xu, Y., Feng, Y., Shi, Y., Li, H., Xing, F., Wang, G., Zhang, Z., & Yi, W. (2025). Monitoring of veterinary drug residues in mutton based on hyperspectral combined with explainable AI: A case study of OFX. Food Chemistry, 474, 143087. https://doi.org/10.1016/j.foodchem.2025.143087.
8. Dufour, É., Frencia, J. P., & Kane, E. (2003). Development of a rapid method based on front-face fluorescence spectroscopy for the monitoring of fish freshness. Food Research International, 36(5), 415–423. https://doi.org/10.1016/S0963-9969(02)00174-6.
9. Duft, R. G., Griffin, J. L., & Stead, D. A. (2025). MEATiCode: A comprehensive proteomic LC-MS/MS method for simultaneous species identification in meat authentication. Food Chemistry, 483, 144231. https://doi.org/10.1016/j.foodchem.2025.144231.
10. Eyre, D. R., Weis, M. A., & Wu, J.-J. (2010). Maturation of collagen ketoimine cross-links by an alternative mechanism to pyridinoline formation in cartilage. Journal of Biological Chemistry,

285(22), 16675–16682. https://doi.org/10.1074/jbc.M110.111534.

11. Fengou, L.-C., Lianou, A., Tsakanikas, P., Mohareb, F., & Nychas, G.-J. E. (2021). Detection of meat adulteration using spectroscopy-based sensors. Foods, 10(4), 861. https://doi.org/10.3390/foods10040861.
12. Gatellier, P., Gomez, S., Gigaud, V., Berri, C., Le Bihan-Duval, E., & Santé-Lhoutellier, V. (2007). Use of a fluorescence front face technique for measurement of lipid oxidation during refrigerated storage of chicken meat. Meat Science, 76(3), 543–547. https://doi.org/10.1016/j.meatsci.2007.01.006.
13. Grispoldi, L., Karama, M., Hadjicharalambous, C., De Stefani, F., Ventura, G., Ceccarelli, M., Revoltella, M., Sechi, P., Crotti, C., & D'Innocenzo, A. (2020). Bovine lymph nodes as a source of Escherichia coli contamination of the meat. International Journal of Food Microbiology, 331, 108715. https://doi.org/10.1016/j.ijfoodmicro.2020.108715.
14. Han, M., Wang, X., Xu, Y., Cui, Y., Wang, L., Lv, D., & Cui, L. (2021). Variable selection for the determination of the soluble solid content of potatoes with surface impurities in the visible/near-infrared range. Biosystems Engineering, 209, 170–179. https://doi.org/10.1016/j.biosystemseng.2021.06.019.
15. Hassoun, A., Alhaj Abdullah, N., Aït-Kaddour, A., Ghellam, M., Beşir, A., Zannou, O., Önal, B., Aadil, R. M., Lorenzo, J. M., & Mousavi Khaneghah, A. (2024). Food traceability 4.0 as part of the fourth industrial revolution: key enabling technologies. Critical Reviews in Food Science and Nutrition, 64(3), 873–889. https://doi.org/10.1080/10408398.2022.2110033.
16. Hassoun, A. (2021). Exploring the potential of fluorescence spectroscopy for the discrimination between fresh and frozen-thawed muscle foods. Photochem, 1(2), 247–263. https://doi.org/10.3390/photochem1020015.
17. Hassoun, A., Sahar, A., Lakhal, L., & Aït-Kaddour, A. (2019). Fluorescence spectroscopy as a rapid and non-destructive method for monitoring quality and authenticity of fish and meat products: Impact of different preservation conditions. LWT, 103, 279–292. https://doi.org/10.1016/j.lwt.2019.01.021.
18. He, Y., Bai, X., Xiao, Q., Liu, F., Zhou, L., & Zhang, C. (2021). Detection of adulteration in food based on nondestructive analysis techniques: A review. Critical Reviews in Food Science and Nutrition, 61(14), 2351–2371. https://doi.org/10.1080/10408398.2020.1777526.
19. Jadeja, R., Teng, X. M., Mohan, A., & Duggirala, K. (2022). Value-added utilization of beef by-products and low-value comminuted beef: Challenges and opportunities. Current Opinion in Food Science, 48, 100938. https://doi.org/10.1016/j.cofs.2022.100938.
20. Jiang, H., Ru, Y., Chen, Q., Wang, J., & Xu, L. (2021). Near-infrared hyperspectral imaging for detection and visualization of offal adulteration in ground pork. Spectrochimica Acta Part A: Molecular and Biomolecular Spectroscopy, 249, 119307. https://doi.org/10.1016/j.saa.2020.119307.
21. Kang, Q., Yu, D., Cheong, K. H., & Wang, Z. (2024). Deterministic convergence analysis for regularized long short-term memory and its application to regression and multi-classification problems.

Engineering Applications of Artificial Intelligence, 133, 108444. https://doi.org/10.1016/j.engappai.2024.108444.

22. Karoui, R., & Blecker, C. (2011). Fluorescence spectroscopy measurement for quality assessment of food systems — a review. Food and Bioprocess Technology, 4(3), 364–386. https://doi.org/10.1007/s11947-010-0370-0.
23. Khamsopha, D., Woranitta, S., & Teerachaichayut, S. (2021). Utilizing near infrared hyperspectral imaging for quantitatively predicting adulteration in tapioca starch. Food Control, 123, 107781. https://doi.org/10.1016/j.foodcont.2020.107781.
24. Kvalheim, O. M., Grung, B., & Rajalahti, T. (2019). Number of components and prediction error in partial least squares regression determined by Monte Carlo resampling strategies. Chemometrics and Intelligent Laboratory Systems, 188, 79–86. https://doi.org/10.1016/j.chemolab.2019.03.006.
25. Lee, G., & Lee, K. (2021). Feature selection using distributions of orthogonal PLS regression vectors in spectral data. BioData Mining, 14(1), 7. https://doi.org/10.1186/s13040-021-00240-3.
26. Leng, T., Hu, X., Chen, Y., Gan, B., Xie, J., & Yu, Q. (2023). Rapid identification and quantitation of pork and duck meat of binary and ternary adulteration in minced beef by 1H NMR combined with multivariate data fusion. Food Control, 154, 110018. https://doi.org/10.1016/j.foodcont.2023.110018.
27. Li, F., Wang, B., Liu, Q., Chen, Q., Zhang, H., Xia, X., & Kong, B. (2019). Changes in myofibrillar protein gel quality of porcine longissimus muscle induced by its structural modification under different thawing methods. Meat Science, 147, 108–115. https://doi.org/10.1016/j.meatsci.2018.09.003.
28. Li, P., Tang, S., Chen, S., Tian, X., & Zhong, N. (2023). Hyperspectral imaging combined with convolutional neural network for accurately detecting adulteration in Atlantic salmon. Food Control, 147, 109573. https://doi.org/10.1016/j.foodcont.2022.109573.
29. Li, Y. C., Liu, S. Y., Meng, F. B., Liu, D. Y., Zhang, Y., Wang, W., & Zhang, J. M. (2020). Comparative review and the recent progress in detection technologies of meat product adulteration. Comprehensive Reviews in Food Science and Food Safety, 19(4), 2256–2296. https://doi.org/10.1111/1541-4337.12579.
30. Liu, T., Zhang, W., Xu, H., Yu, J., Sang, T., Wang, Y., & Wang, S. (2025). Non-destructive quantitative detection of lymphatic meat adulterated in beef by hyperspectral imaging combined with interpretable deep learning. Food Control, 181, 111742. https://doi.org/10.1016/j.foodcont.2025.111742.
31. Monago-Maraña, O., Wold, J. P., Rødbotten, R., Dankel, K. R., & Afseth, N. K. (2021). Raman, near-infrared and fluorescence spectroscopy for determination of collagen content in ground meat and poultry by-products. LWT, 140, 110592. https://doi.org/10.1016/j.lwt.2020.110592.
32. Oleinikova, Y., Maksimovich, S., Khadzhibayeva, I., Khamedova, E., Zhaksylyk, A., & Alybayeva, A. (2025). Meat quality, safety, dietetics, environmental impact, and alternatives now and ten years ago: A critical review and perspective. Food Production, Processing and Nutrition, 7(1), 18. https://doi.org/10.1186/s43014-024-00305-w.

33. Pearce, E. L., & Pearce, E. J. (2013). Metabolic pathways in immune cell activation and quiescence. Immunity, 38(4), 633–643. https://doi.org/10.1016/j.immuni.2013.04.005.
34. Peng, S., Fan, L., Zhang, L., Su, H., He, Y., He, Q., Wang, X., Yu, D., & Zhang, J. (2024). Spatio-temporal prediction of total energy consumption in multiple regions using explainable deep neural network. Energy, 301, 131526. https://doi.org/10.1016/j.energy.2024.131526.
35. Pu, K., Qiu, J., Tong, Y., Liu, B., Cheng, Z., Chen, S., Ni, W.-X., Lin, Y., & Ng, K.-M. (2023). Integration of non-targeted proteomics mass spectrometry with machine learning for screening cooked beef adulterated samples. Journal of Agricultural and Food Chemistry, 71(4), 2173–2182. https://pubs.acs.org/doi/10.1021/acs.jafc.2c06266.
36. Rinnan, Å., Van Den Berg, F., & Engelsen, S. B. (2009). Review of the most common pre-processing techniques for near-infrared spectra. TrAC Trends in Analytical Chemistry, 28(10), 1201–1222. https://doi.org/10.1016/j.trac.2009.07.007.
37. Saleem, A., Sahar, A., Pasha, I., & Shahid, M. (2022). Determination of adulteration of chicken meat into minced beef mixtures using front face fluorescence spectroscopy coupled with chemometric. Food Science of Animal Resources, 42(4), 672–688. https://doi.org/10.5851/kosfa.2022.e29.
38. Saleem, A., Imtiaz, A., Yaqoob, S., Awais, M., Awan, K. A., Naveed, H., Khalifa, I., Al-Asmari, F., & Qian, J. Y. (2024). Integration of fluorescence spectroscopy along with mathematical modeling for rapid prediction of adulteration in cooked minced beef meat. Journal of Food Process Engineering, 47(12), e70003. https://doi.org/10.1111/jfpe.70003.
39. Üstün, B., Melssen, W., & Buydens, L. (2007). Visualisation and interpretation of support vector regression models. Analytica Chimica Acta, 595(1–2), 299–309. https://doi.org/10.1016/j.aca.2007.03.023.
40. Vohra, P., Bugarel, M., Turner, F., Loneragan, G. H., Hope, J. C., Hopkins, J., & Stevens, M. P. (2018). Quantifying the survival of multiple Salmonella enterica serovars in vivo via massively parallel whole-genome sequencing to predict zoonotic risk. Applied and Environmental Microbiology, 84(4), e02262-17. https://doi.org/10.1128/AEM.02262-17.
41. Wang, G., Yan, X., Feng, Y., Chen, Y., Cui, J., Liu, S., & Wang, S. (2025). Deep learning-driven hyperspectral imaging for real-time monitoring and growth modeling of psychrophilic spoilage bacteria in chilled beef. International Journal of Food Microbiology, 439, 111254. https://doi.org/10.1016/j.ijfoodmicro.2025.111254.
42. Wang, W., Jiang, F., Wu, W. Q., Zhu, X. L., Wang, H.-X., Zhang, L., & Fan, Z.-Y. (2024). Identification of lymph node adulteration in minced pork by comprehensive metabolomics and lipidomics approach based on UPLC/LTQ-Orbitrap MS. Journal of Food Science, 89(4), 2249–2260. https://doi.org/10.1111/1750-3841.17005.
43. Weng, S., Guo, B., Tang, P., Yin, X., Pan, F., Zhao, J., Huang, L., & Zhang, D. (2020). Rapid detection of adulteration of minced beef using Vis/NIR reflectance spectroscopy with multivariate methods. Spectrochimica Acta Part A: Molecular and Biomolecular Spectroscopy, 230, 118005. https://doi.org/10.1016/j.saa.2019.118005.

44. Yang, C., Zhong, G., Zhou, S., Guo, Y., Pan, D., Wang, S., Liu, Q., Xia, Q., & Cai, Z. (2022). Detection and characterization of meat adulteration in various types of meat products by using a high-efficiency multiplex polymerase chain reaction technique. Frontiers in Nutrition, 9, 979977. https://doi.org/10.3389/fnut.2022.979977.
45. Yu, Y., Chen, W., Zhao, D., Zhang, H., Chen, W., Liu, R., & Li, C. (2025). Meat species authentication using portable hyperspectral imaging. Frontiers in Nutrition, 12, 1577642. https://doi.org/10.3389/fnut.2025.1577642.
46. Yuan, Y., Ji, Z., Fan, Y., Xu, Q., Shi, C., Lyu, J., & Ertbjerg, P. (2025). Deep learning-assisted fluorescence spectroscopy for food quality and safety analysis. Trends in Food Science & Technology, 156, 104821. https://doi.org/10.1016/j.tifs.2024.104821.
47. Zhang, J., & Yang, H. (2025). Robust support vector machine based on the bounded asymmetric least squares loss function and its applications in noise corrupted data. Advanced Engineering Informatics, 65, 103371. https://doi.org/10.1016/j.aei.2025.103371.
48. Zhang, P., Wang, H., Klima, C., & Yang, X. (2024). Microbiota in lymph nodes of cattle harvested in a Canadian meat processing plant. Food Research International, 191, 114693. https://doi.org/10.1016/j.foodres.2024.114693.
49. Zhao, X., Wang, L., Zhang, Y., Han, X., Deveci, M., & Parmar, M. (2024). A review of convolutional neural networks in computer vision. Artificial Intelligence Review, 57(4), 99. https://doi.org/10.1007/s10462-024-10721-6.

Figures

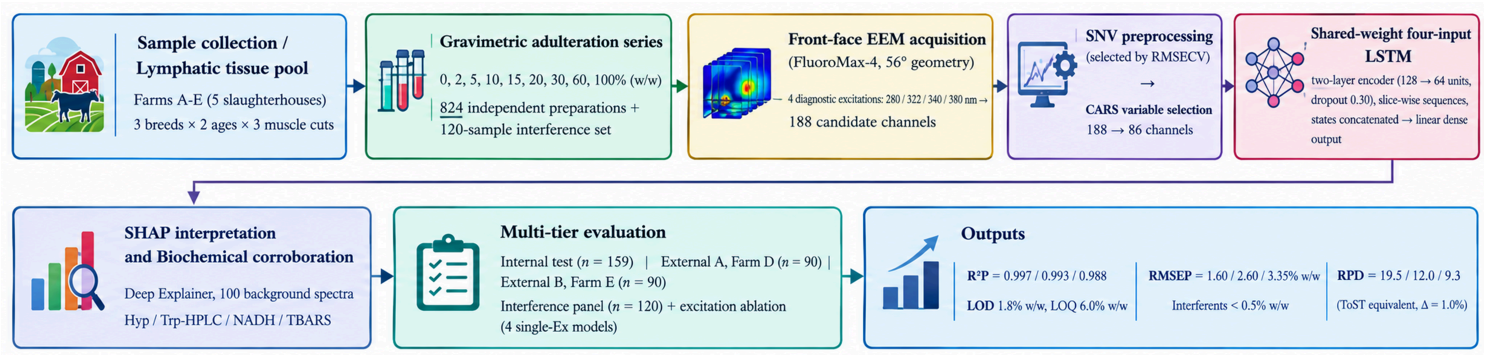


Figure 1

Schematic overview of the experimental workflow, from multi-farm sample collection (Farms A-E) and the gravimetric adulteration series (0-100% w/w lymphatic tissue), through front-face EEM acquisition at four diagnostic excitation wavelengths (280, 322, 340 and 380 nm), SNV preprocessing, CARS variable selection, shared-weight four-input LSTM modelling, and SHAP interpretation with biochemical corroboration.

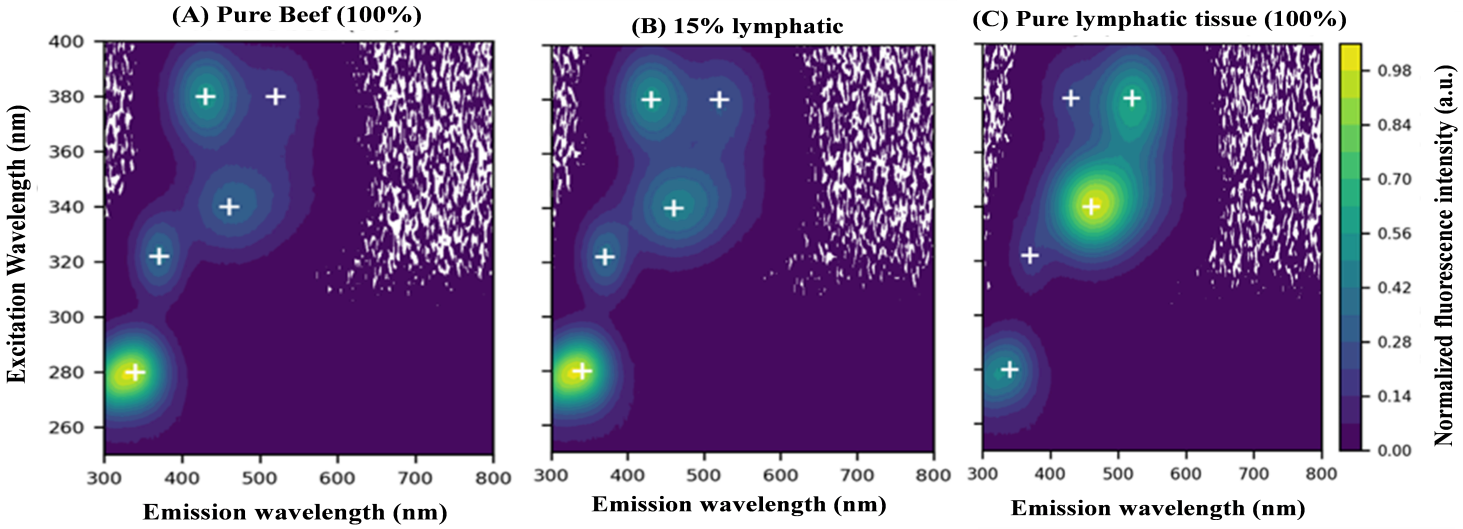


Figure 2

Representative excitation-emission matrices (EEMs) for (A) pure beef (0% adulteration), (B) 15% lymphatic adulteration and (C) 100% pure lymphatic tissue. White crosses mark the five diagnostic fluorophore regions. The bidirectional spectral changes between pure beef and lymphatic tissue confirm a unique biochemical fingerprint rather than simple dilution. Colour scale: fluorescence intensity in arbitrary units (a.u.).

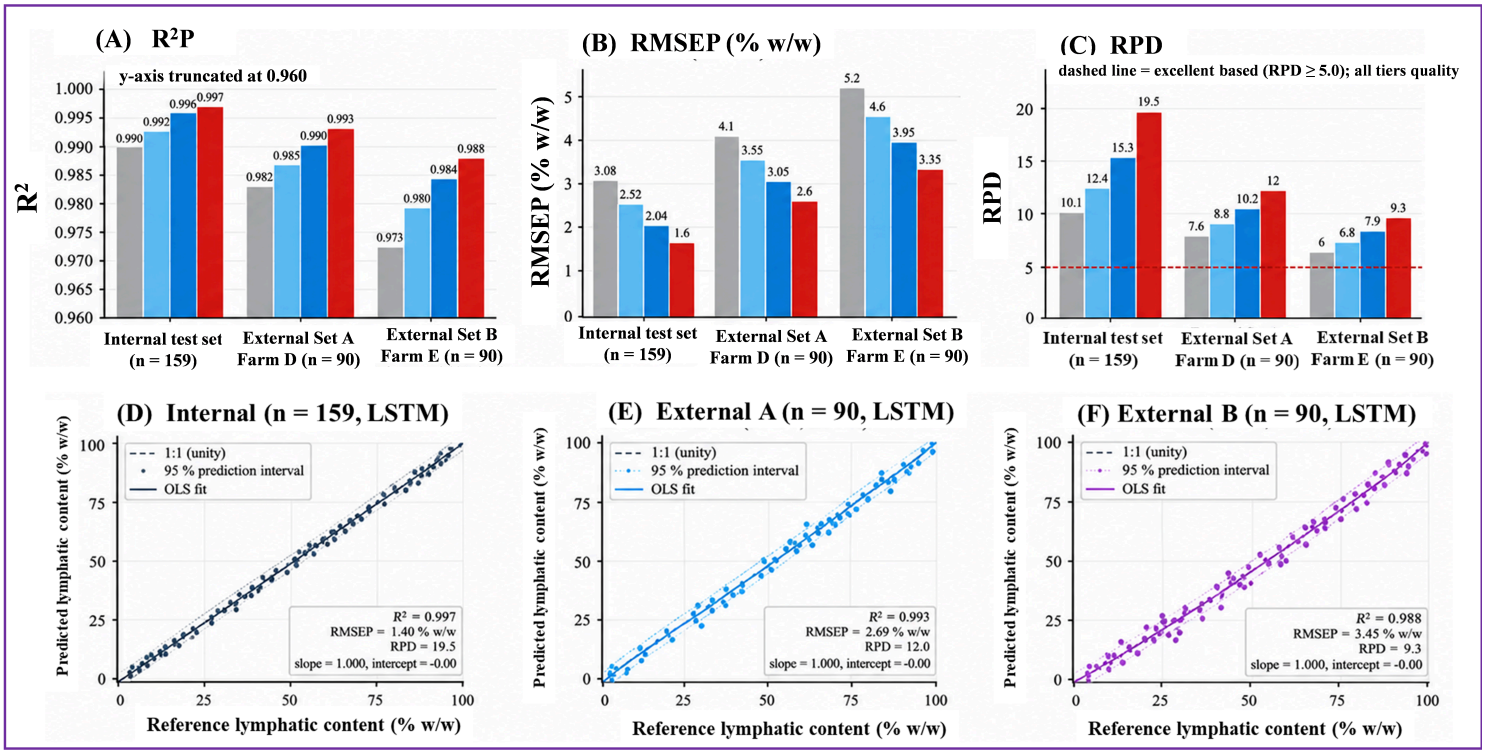


Figure 3

Comparative model performance and multi-level validation. (A-C) R^2P, RMSEP (% w/w) and RPD for PLSR, LSSVM, 1D-CNN and LSTM on the internal test set (n = 159), External Set A (Farm D; n = 90) and External

Set B (Farm E; n = 90); bars are means across five random seeds. The LSTM led every tier (RMSEP 1.60, 2.60 and 3.35 % w/w; RPD 19.5, 12.0 and 9.3), though by only ΔR^2P = 0.001-0.004 over the 1D-CNN, and every tier stayed within the excellent band (RPD ≥ 5.0, dashed line in C). (D-F) Reference versus predicted plots for the LSTM, with 1:1 line (dashed), least-squares fit (solid) and 95 % prediction interval (shading). (G) Bootstrap 95 % CIs of RMSEP (10,000 resamples): the internal interval (1.44-1.75 % w/w) does not overlap either external interval (2.21-2.97 and 2.87-3.84 % w/w), and the seed-to-seed SD (0.07 % w/w, horizontal bar) is far narrower than these intervals. Reference SD = 31.2 % w/w in each set. PLSR, partial least squares regression; LSSVM, least-squares support vector machine; 1D-CNN, one-dimensional convolutional neural network; LSTM, long short-term memory.

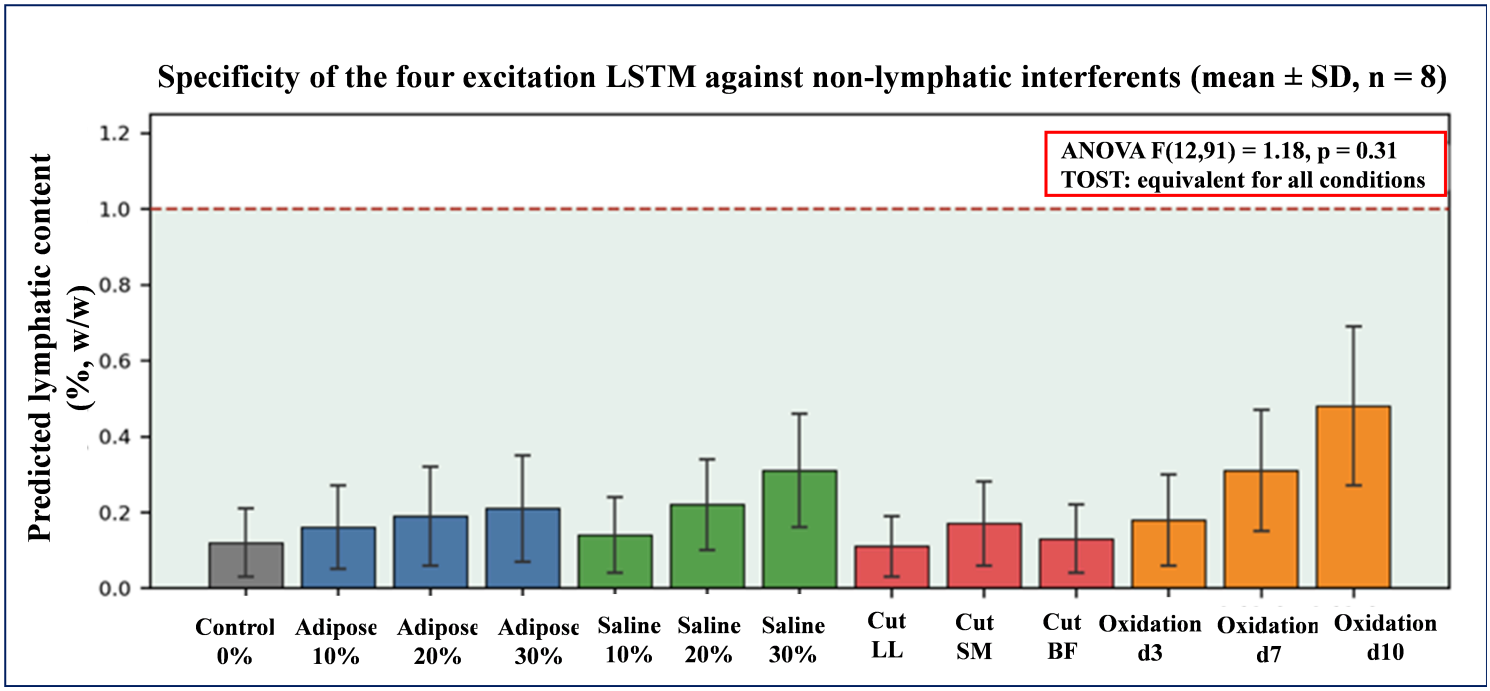


Figure 4

Specificity of the LSTM model against four non-lymphatic interferent categories. Predicted lymphatic tissue content (% w/w; mean ± SD, n = 8) for authentic beef (0%), adipose tissue (10, 20 and 30%), saline dilution (10, 20 and 30%), muscle-cut variation (LL, SM and BF at 0% adulteration) and lipid oxidation (3, 7 and 10 days at 4 °C). All mean predicted values remained below 0.5% w/w. One-way ANOVA with Tukey HSD showed no significant difference from control; TOST confirmed equivalence within ±1.0% w/w.

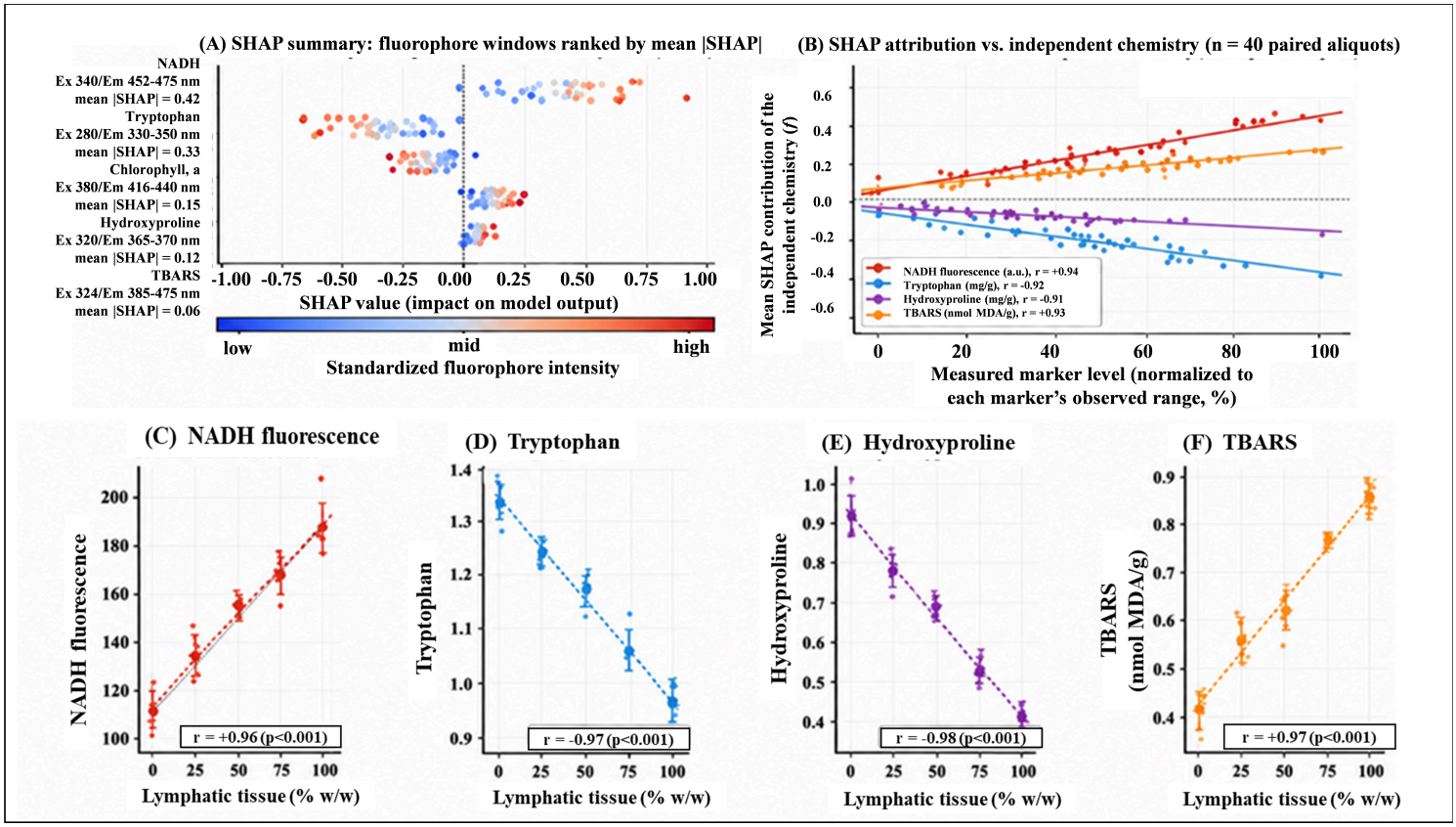


Figure 5

SHAP feature-importance ranking for the trained LSTM model. Bars give the mean absolute SHAP value (arbitrary units) per fluorophore region, ordered by decreasing importance. Red bars denote a positive SHAP effect (higher feature value → higher predicted adulteration); blue bars denote a negative SHAP effect. Excitation/emission assignments are labelled on the y-axis and cross-checked against the biochemical assays in Tables S5 and S6. Mean ± SD (n = 6 per level) (C) NADH fluorescence (D) tryptophan, (E) hydroxyproline, and (F) TBARS at 0, 25, 50, 75 and 100% (w/w) lymphatic tissue. All four markers change monotonically, matching the sign of the corresponding SHAP effect

Agreement at the two extremes does not show that the markers track adulteration continuously, so an independent dose series was assayed at 0, 25, 50, 75 and 100% (w/w) lymphatic tissue (n = 6 independent preparations per level; Table S6, Supplementary Figure S3). All four markers changed monotonically and near-linearly across the range, with correlations against gravimetric adulteration level of |r| = 0.96-0.98 (n = 30 per marker, $p < 0.001$; the 0% and 100% levels are the shared endpoint batches described in Section 2.6). The endpoint values of the dose series reproduced those of Table S5, and the direction of every marker matched the sign of the corresponding SHAP effect. The biochemical corroboration therefore holds across the 0-100% range, not only at its endpoints.

Supplementary Files

This is a list of supplementary files associated with this preprint. Click to download.

- Supplementarymateriallegends.docx
- 7.Supplementarymaterial.docx